ISPRS Journal of Photogrammetry and Remote Sensing 193 (2022) 77–89

Contents lists available at ScienceDirect

ISPRS Journal of Photogrammetry and Remote Sensing

journal homepage: www.elsevier.com/locate/isprsjprs

Developing a sub-meter phenological spectral feature for mapping poplars and willows in urban environment

Xiangcai Li [a], Jinyan Tian [a,*], Xiaojuan Li [a], Le Wang [b], Huili Gong [a], Chen Shi [a], Sheng Nie [c], Lin Zhu [a], Beibei Chen [a], Yun Pan [a], Jijun He [a], Rongguang Ni [d], Chunyuan Diao [e,*]

[a] Beijing Laboratory of Water Resources Security, Capital Normal University, Beijing, China
[b] Department of Geography, The State University of New York at Buffalo, Buffalo, NY, USA
[c] Key Laboratory of Digital Earth Science, Aerospace Information Research Institute, Chinese Academy of Sciences, Beijing, China
[d] State Key Laboratory of Remote Sensing Science, Institute of Remote Sensing Science and Engineering, Faculty of Geographical Science, Beijing Normal University, Beijing, China
[e] Department of Geography and Geographic Information Science, University of Illinois at Urbana-Champaign, IL, USA

ARTICLE INFO

Keywords:
Urban
Tree species classification
Phenology
Sub-meter
Multi-scale
Deep learning

ABSTRACT

Poplar and willow catkins (PWCs) have caused severe impacts on human health and environmental quality, and accurate poplars and willows (PaWs) mapping with remote sensing is essential to monitor and manage the PWCs. However, two major issues have constrained the urban tree species (e.g. PaWs) identification: (1) the urban tree landscapes are highly fragmented and susceptible to the existence of mixed pixels in the remote sensing imagery; (2) the tree species in urban environment are diverse with high spectral similarity. To this end, this study developed a sub-meter phenological spectral feature (Spsf) with multi-scale and multi-temporal remote sensing imagery for monitoring PaWs at the tree species level.

Spsf includes three steps: (1) exploring three key phenological periods of PaWs (leafless period, greenleaf period, and senescence period); (2) selecting one or three spectral indexes to characterize each phenological period; (3) stacking the spectral vegetation indexes from Sentinel-2 SR imagery and freely available sub-meter (0.8 m) Google Earth imagery together. Subsequently, Spsf was taken as the input data to train the deep learning DeepLabv3 + model for predicting the PaWs distribution. The Beijing Plain was chosen as the study area, where the distribution of PaWs was extensive and fragmented. Compared with the field survey reference data, the derived PaWs map achieved the overall accuracy higher than 92 % and the Kappa coefficient of 0.83. The Spsf integrated rich spatial information from sub-meter imagery and phenological spectral information from Sentinel-2 imagery, which may alleviate the impacts of mixed pixels and enhance the spectral separability between PaWs and other tree species effectively. The proposed Spsf-based method provides a new paradigm for sub-meter tree species mapping with multi-source free remote sensing data. The PaWs map can serve as reference data for the relevant departments to monitor and manage the PWCs.

1. Introduction

Poplars and willows (PaWs), belonging to the *Salicaceae* family, are widely planted in many countries because of the benefits of alleviating climate change, preventing soil erosion, rehabilitating degraded land, and sequestering carbon (Felix et al., 2008; Gordon, 2001; Isebrands and Richardson, 2014; Pulford and Watson, 2003). But there are still some negative impacts of planting PaWs, among which is the potential environmental and health issue caused by the poplars and willows catkins (PWCs). PWCs are the seed hairs attached to the seeds after the capsules of the female plants of poplar and willow trees become mature (Li et al., 2016). The appearance of PWCs may pose significant threats to human health and environmental quality because it can cause allergic reactions, respiratory diseases, and environmental pollution (Wan et al., 2020). Given the circumstances aforementioned, it is necessarily important to monitor the distribution of PaWs for effective management

* Corresponding authors.
E-mail addresses: 2200902201@cnu.edu.cn (X. Li), tjyremote@126.com (J. Tian), lixiaojuan@cnu.edu.cn (X. Li), lewang@buffalo.edu (L. Wang), 4039@cnu.edu.cn (H. Gong), 6506@cnu.edu.cn (C. Shi), niesheng@aircas.ac.cn (S. Nie), 5533@cnu.edu.cn (L. Zhu), 6183@cnu.edu.cn (B. Chen), 5850@cnu.edu.cn (Y. Pan), 5815@cnu.edu.cn (J. He), rongguangni@gmail.com (R. Ni), chunyuan@illinois.edu (C. Diao).

https://doi.org/10.1016/j.isprsjprs.2022.09.002
Received 23 June 2022; Received in revised form 8 August 2022; Accepted 2 September 2022
Available online 15 September 2022

of PWCs.

The traditional field surveys are time and labor-intensive, economically expensive, and difficult to implement, especially on a regional scale to carry out tree species monitoring (Kulawardhana et al., 2014; Rana et al., 2016). On the contrary, remote sensing performs more efficiently in long-term regional and global tree species mapping (Jia et al., 2016; Moreau et al., 2003; Rana et al., 2016). According to the spatial resolution, the optical data applied to tree species detection can be divided into three categories: medium–high resolution data (e.g., Sentinel), high-resolution data (e.g., SPOT 5–7), and very high-resolution (VHR) data (e.g., unmanned aerial vehicle, WorldView). The medium–high resolution data has been applied in PaWs mapping in forest areas (Hamrouni et al., 2021; Tonbul et al., 2020), but obstacle exists when such type of data are utilized in urban areas: the complex composition of urban trees in highly fragmented urban environment is subject to the issue of the mixed pixels, which may lead to poor mapping accuracy. The high-resolution and VHR data have provided opportunities for accurate mapping of tree species (Korznikov et al., 2021; Noonan and Chafer, 2007), yet almost all those types of data are typically economically expensive and usually confined to limited spatial extents and temporal coverage, making the large-scale mapping of PaWs difficult (Berni et al., 2009; Fassnacht et al., 2016; Tian et al., 2017).

Fortunately, the VHR remote sensing imagery freely available from Google Earth (GE) provides a new idea for fragmented PaWs mapping. The global historical images at a sub-meter resolution can be acquired by the GE platform openly (Geng et al., 2020; Hu et al., 2013), which may break the barriers in tree species mapping at large scales due to the acquisition cost of typical commercial high-resolution and VHR imagery becoming prohibitively expensive. Additionally, the GE imagery contains fine-grained spatial details such as shape, texture, and context, which are particularly critical for urban landscapes (Mura et al., 2008). Recently, several studies have attempted to leverage GE imagery for tree species detection (Dong et al., 2019; Fang et al., 2020). For instance, Guirado et al. (2017) utilized the GE images to perform accurate *Ziziphus lotus* mapping based on the ResNet classifier, a transferable Convolutional Neural Network (CNN) model, and achieved the F1 score of 96.50 %. Nonetheless, the application of GE imagery in tree species mapping is still constrained, particularly due to the limited spectral information. Since the GE imagery only contains the red, green, and blue (RGB) bands, the poor spectral information may inevitably prevent the use of effective bands or derived indexes for accurate tree detection (Huete et al., 1997; Tucker, 1979).

In addition to the spatial resolution consideration, the phenological information also has significant effects on improving the accuracy of tree species mapping (Evangelista et al., 2009; Fang et al., 2018; Lu and Wang, 2021; Pu et al., 2018). Different tree species possess their specific phenological trajectories. The unique spectral characteristics that trees present in their phenological periods (i.e., leafless period, senescence period) may enhance the spectral separability between the target tree species and others (Li et al., 2021; Wang et al., 2013). Historically, single key phenological period was considered helpful for tree species detection (Li et al., 2021; Masemola et al., 2020), for example, Ji and Wang (2016) employed the composite images during the coloration period of an invasive species (i.e., saltcedar) to monitor its distribution in the western U.S., and obtained an overall accuracy of higher than 93 %. However, two issues may exist with the leverage of single key phenological period for PaWs detection: (1) the single key phenological period can hardly encompass all the distinct spectral characteristics of PaWs over a growth cycle. Spectral confusion may exist if the target tree species and other species present similar spectral characteristics during this period, especially in the heterogeneous urban environment; (2) the single period may suffer from poor robustness to perform tree species detection. Image unavailability or poor image quality during this period will make it difficult to guarantee the classification accuracy. Alternatively, the time series images have been proved to be more efficient in tree species mapping (Grabska et al., 2019; Kollert et al., 2021; Pastor-Guzman et al., 2018). For example, Diao and Wang (2016) employed the monthly time series images to establish the phenological trajectory of saltcedar (*Tamarix* spp.), and achieved an overall accuracy of 88.54 %, which had proved the effectiveness and robustness of time series images in tree species mapping. However, there are still limitations which may hamper the mapping precision: (1) the monthly time-series images cannot capture the intra-month variations in vegetation phenology. Since the vegetation phenological periods may vary drastically within a month time, using monthly time series images may lose information about the changes in vegetation phenological periods, thus drastically impacting the detection accuracy; (2) sufficient images to construct the phenological trajectory are difficult to guarantee. Limited by the satellite revisit cycles and cloud contamination issues, it is usually difficult to acquire sufficient time series images to support such a tree species detection strategy. Recently, researches have strived to utilize the multiple key phenological periods for invasive species or crops monitoring. Multiple key phenological periods rely fewer on images and can reflect the phenological characteristics more comprehensively. It has been utilized in monitoring invasive species or paddy rice (Ni et al., 2021; Wu et al., 2020). However, there is no study applying the multiple key phenological period-based detection strategy to tree species mapping, let alone in the highly heterogeneous urban environment.

Therefore, the objective of this study was to develop a PaWs detection strategy by stacking the spatial feature from sub-meter imagery and the multiple key phenological features from Sentinel-2 imagery. More specifically, we strived to: (1) develop a sub-meter phenological spectral feature (Spsf) to make full use of the spatial information of free sub-meter remote sensing images and the spectral information of multiple key phenological periods; (2) conduct the sub-meter accurate mapping of PaWs in the Beijing Plain for the first time. In short, this study not only advanced the method development for urban tree species classification, but also broke the barriers associated with high cost of sub-meter species mapping. This study can thus facilitate the shaping of a new paradigm for sub-meter tree species mapping. The derived PaWs map can serve as a basic reference data for relevant departments in the monitoring and managing of PaWs.

2. Study area and data

2.1. Study area

The Beijing Plain, located in the southeast of Beijing (39.28°N to 41.05°N and 115.25°E to 117.35°E), is the study area of this research (Fig. 1). PaWs, as the major species for the Beijing Plain, have been widely planted for sightseeing, producing wood, and combating desertification. However, the PWCs have caused serious troubles to people's lives and environment. When people are exposed to the environment of PWCs, they are prone to allergic reactions and respiratory diseases. The distribution characteristics of PaWs in the Beijing Plain, such as severe fragmentation, surrounded by a diversity of other tree species, and high spectral similarity between PaWs and surrounding species, have made it difficult to acquire the accurate mapping of PaWs. To date, there is no accurate mapping product for the distribution of PaWs in the Beijing Plain.

2.2. Datasets

2.2.1. Remote sensing imagery

The remote sensing images used in this study mainly include the GE imagery and Sentinel-2 imagery: (1) GE 19 level remote sensing imagery with a spatial resolution of 0.56 m was adopted. In view of the diversity of GE data sources, the partitioned strategy was applied to obtain data with the aim to ensure the data quality. The entire study area was divided into the 10*10 fishnet with a total of 100 subareas. For each subarea, we filtered the images with the least cloudiness from the 2019 ~ 2020 summer images. Then all the subarea images were mosaicked

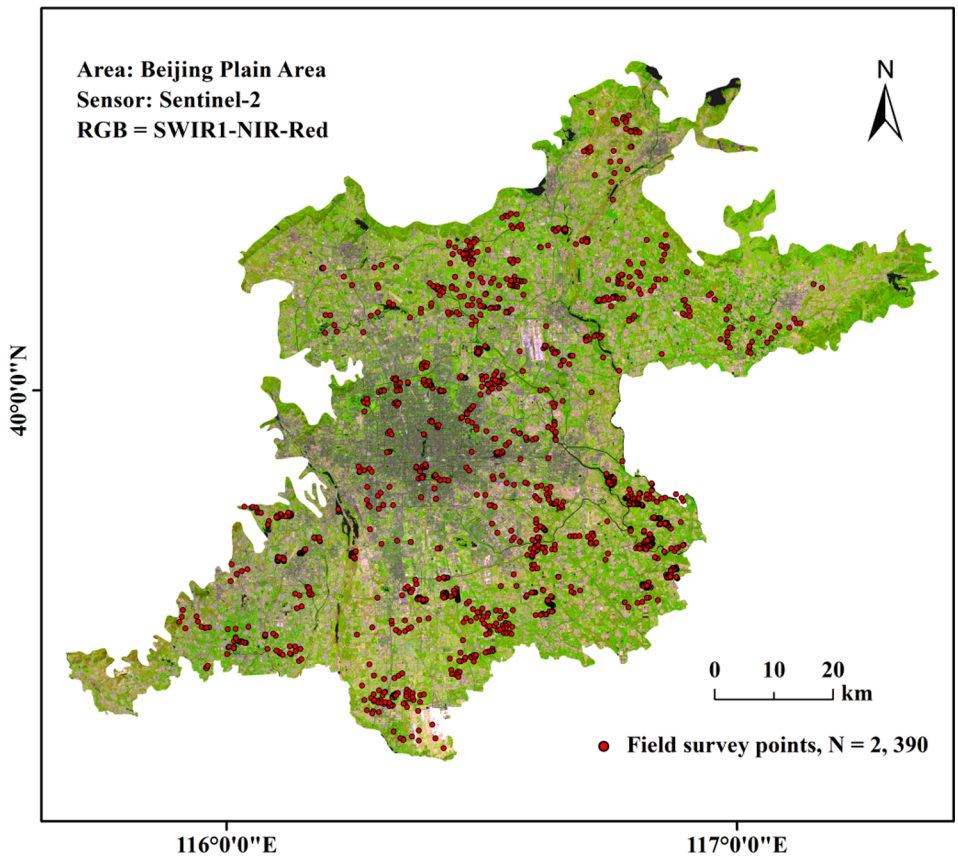

Fig. 1. The Sentinel-2 SR image of Beijing Plain, the red points represent the distribution of 2,390 field survey sample points. (For interpretation of the references to color in this figure legend, the reader is referred to the web version of this article.)

into a complete image of the entire study area in ArcGIS 10.2. Ten typical regions were chosen from the GE imagery as the samples used in the deep learning (DL) model. For each region, the unsupervised multi-resolution segmentation was performed in eCognition Developer 64 (eCognition Developer, 2014) to acquire image feature objects, and then all the image objects of each typical region were assigned land cover attributes manually; (2) all the available Sentinel-2 surface reflectance (SR) images covering the whole study area were taken as the input data to analyze the spectral characteristics of PaWs during the distinct phenological periods. And we acquired the images from the Google Earth Engine (GEE) throughout the whole year of 2019 ~ 2020. Meanwhile, the summer RGB bands of Sentinel-2 SR images from 2019 ~ 2020 were also used in this study.

2.2.2. Field survey data

The field survey data were obtained from two aspects. The first aspect was through field measurements in the summer of 2020. We recorded the coordinates of PaWs through the GPS device and took field photos in the Beijing Plain. The second aspect was via the Baidu Street View Maps. The Baidu Street View application programming interface (API) was leveraged to achieve massive Street View data acquisition, which facilitates the expansion of field survey data. In total, we obtained 2,390 sample points in the Beijing Plain (Fig. 1), including 1,500 PaWs samples and 890 non-PaWs samples, and these points were distributed evenly in our study area. Among these samples, half of the PaWs sample points (750 points) and half of the non-PaWs sample points (445 points) were used to assist in obtaining the DL training samples, and the remaining PaWs and non-PaWs sample points were used for accuracy validation of the DL prediction results.

2.2.3. DL training data

The object-based method was used for generating DL training labels, and the process can be divided into three steps: (1) performing the unsupervised multi-resolution segmentation in ten typical regions to obtain the image objects; (2) the image objects were assigned land cover attributes manually according to the prior knowledge, along with the Baidu Street View Map and field survey data; (3) all the samples were split into labels of size 512*512 to perform DL training.

The unsupervised multi-resolution segmentation, applied to generate image objects in eCognition Developer 64 (eCognition Developer, 2014) is a bottom-up region merging technique (Dorren et al., 2003). The larger the segmentation scale, the larger the merged image objects, and vice versa. The larger the segmentation scale, the smaller the total number of image objects and the lower the purity of the land cover in an image object. However, too small segmentation scale may lead to an excessive number of image objects, resulting in redundant information. Consequently, an optimal segmentation scale is critical. According to the visual interpretation and previous research (Johnson and Xie, 2011; Wang et al., 2021), 21 segmentation scales ranging from 20 to 100 with the step of 4 were utilized to perform multi-resolution segmentation. The optimal segmentation scale was identified through the criteria of the maximum inter-object heterogeneity and the intra-object homogeneity (Johnson and Xie, 2011; Zhang et al., 2008). Finally, the optimal segmentation scale was determined with the minimum global score (GS) value, and the details of calculating GS can be found in our previous study (Wang et al., 2021).

The optimal segmentation scales of the ten typical areas were presented in a histogram (Fig. 2). The optimal scales for the ten areas were 68, 52, 80, 68, 32, 44, 44, 40, 68, and 48, respectively. Each typical area was segmented according to the optimal segmentation scale to generate the image objects which were subsequently utilized for obtaining the DL

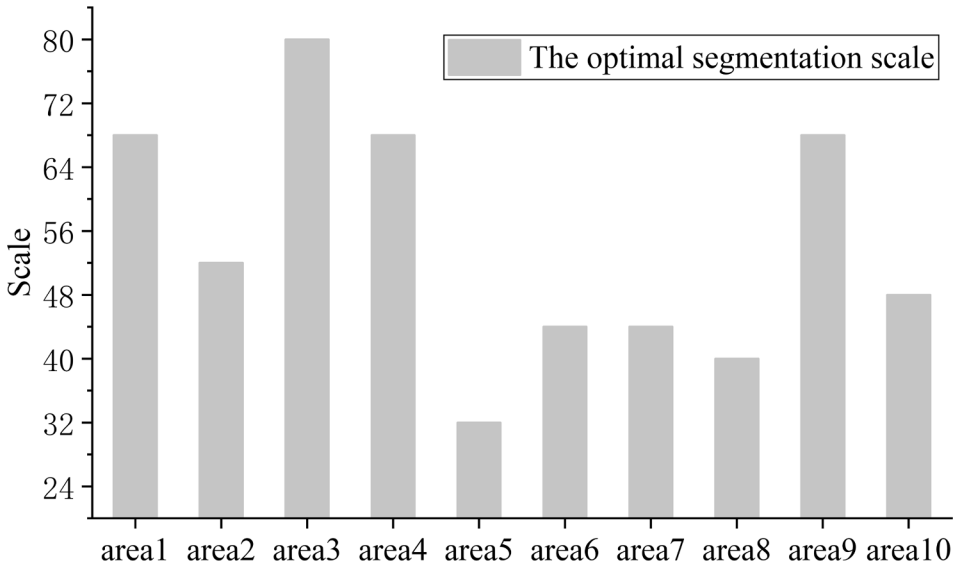

Fig. 2. The optimal segmentation scales of the ten typical areas.

samples.

Based on the image objects obtained by the optimal segmentation scale, the DL training and samples were generated by assigning land cover attributes to the image objects in ArcGIS 10.2. All the ten typical areas performed the above operations similarly. Subsequently, all the samples were split into labels of size 512*512. Since the pixels on the edge of labels contain fewer contextual information, which may lead to unreliable predictions for these pixels, all labels were set with an overlap rate of about 15 % when cropped out of the samples (Chen et al., 2018). Finally, 1,100 labels were acquired as the input data for performing DL training. All the labels were evenly distributed in the study area.

2.2.4. Accuracy validation data

After the DL training and prediction, necessary accuracy validation was performed on the derived mapping products. The field survey sample points, including 750 PaWs samples and 445 non-samples were used for accuracy validation. And the assessment metrics used in this study were the overall accuracy (OA), producer accuracy (PA), user accuracy (UA), and the Kappa coefficient.

3. Methods

The methods used in this research include three parts. First, the Spsf-based method was developed to acquire a new feature which incorporated the three key phenological periods of PaWs and GE sub-meter image. Second, comparative experiment was performed to evaluate the improvement in spectral separability with Spsf. Third, the Spsf-based composite image was taken as the input data for DL DeepLabv3 + training and obtaining the PaWs distribution of the Beijing Plain.

3.1. The sub-meter phenological spectral feature (Spsf)

There were three main steps to applying the Spsf-based method: (1) cloud masking was performed on the Sentinel-2 SR imagery to reduce the impact of cloudiness on image quality (2) exploring three key phenological periods of PaWs by analyzing the temporal profile of Green Chlorophyll Vegetation Index (GCVI) (Gitelson et al., 2003), Normalized Difference Vegetation Index (NDVI) (Tucker, 1979), and Plant Senescence Reflectance Index (PSRI) (Merzlyak et al., 1999) during 2019 ~ 2020; (3) selecting one or three spectral vegetation indexes for characterizing each key phenological period. The Spsf was developed by compositing the GE sub-meter imagery and the characterized three key phenological periods imagery. The flowchart of Spsf can be seen in Fig. 3.

3.1.1. Cloud masking

With the purpose of reducing the impact of cloudiness on image quality, cloud masking should be carried out prior to the analysis of the Sentinel-2 SR imagery. First, for the entire scene, the image property taken from the metadata, CLOUDY_PIXEL_PERCENTAGE, was used to screen out the images with more than 70 % cloud volume with reference to the previous research (Hermosilla et al., 2016). The opaque and cirrus cloud pixels were further masked off with the cloud information in the bit 10 and bit 11 of the QA60 bitmask embedded in the Sentinel-2 imagery, respectively.

3.1.2. Identifying the key phenological periods of PaWs

The analysis of PaWs phenological periods was implemented in GEE using the time series of Sentinel-2 SR images, and the temporal profiles of GCVI, NDVI, and PSRI were acquired to analyze the key phenological periods of PaWs. The temporal profiles of the three indexes were derived by calculating 150 pure PaWs sample points evenly distributed in the study area on all available cloud masked images from Jan. 2019 to Dec. 2020. The days in 2019 ~ 2020 were mosaicked into one year and ordered by Day of Year (DoY) for acquiring enough available images and reducing the impacts of extreme weather. It is important to note that as for the tree species with high interannual variability in phenological periods, it would be a better choice to apply the one-year image when enough images are available. At the same time, we calculated the median value of all the raw values on each DoY. Clouds and atmospheric conditions, however, can cause remote sensing time series imagery to be contaminated by noise (Pastor-Guzman et al., 2018). Therefore, necessary operations should be performed to smooth the time series images before the subsequent analysis. The Savitzky-Golay (SG) algorithm (Savitzky and Golay, 1964), a polynomial smoothing algorithm based on the principle of least-squares, had been proved to be more robust and efficient in reducing the contamination caused by clouds and the atmosphere from time-series imagery (Chen et al., 2004). Therefore, in this research, all the median values of DoY were smoothed by the SG algorithm to generate the average annual profile. According to the previous research (de Castro et al., 2018; Ni et al., 2021) and the characteristics of the median values of all PaWs vegetation indexes, the smoothing window and degree of smoothing polynomial were set to be 20 and 2, respectively. The smoothed temporal profiles of the three indexes were shown in Fig. 4. The grey points represent the raw values of different index values. The blue line represents the median value of all

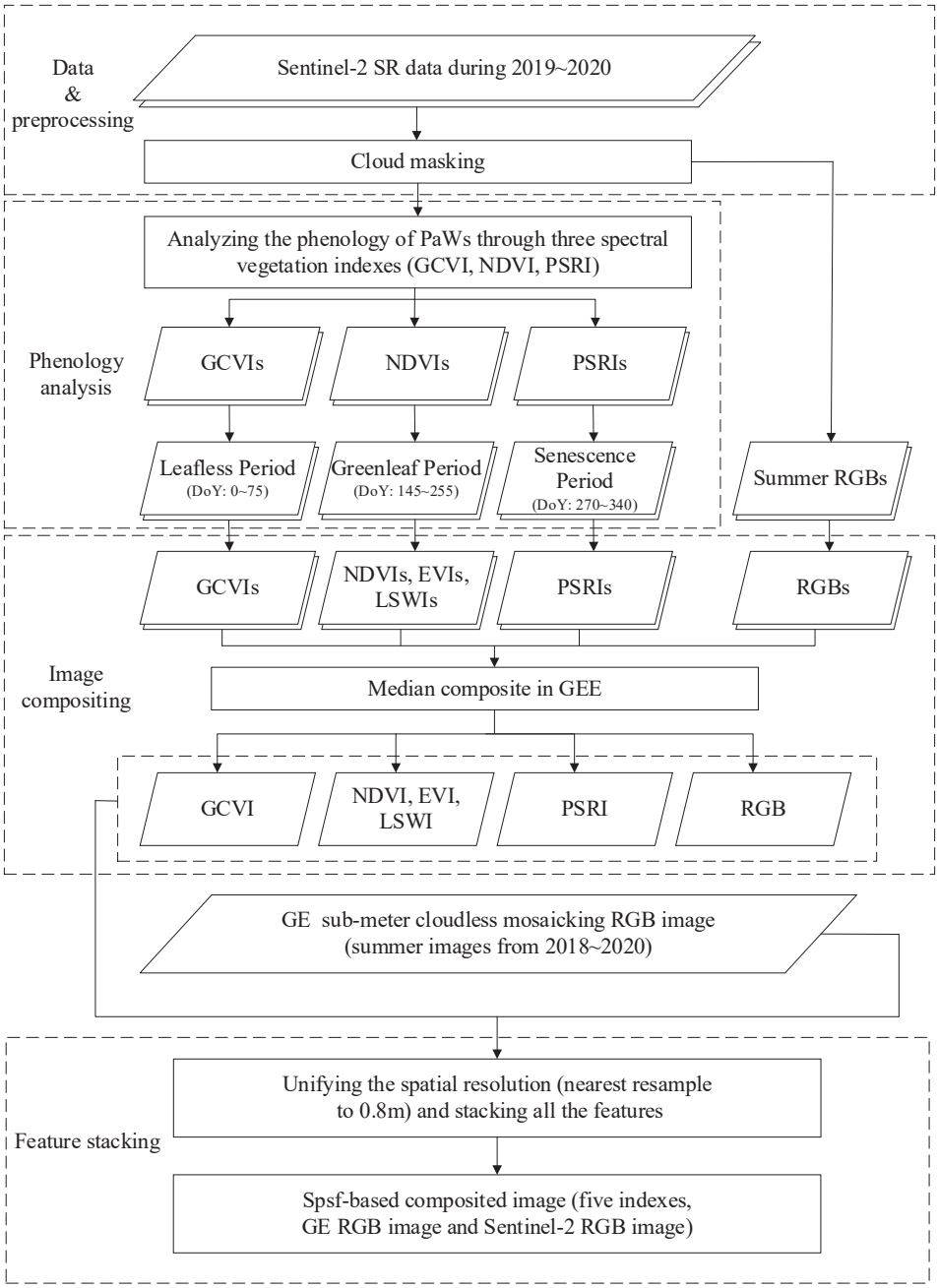

Fig. 3. The flowchart of proposed Spsf.

the grey points of each DoY, and the red line indicates the smoothed result of the median value by the SG algorithm. The reasons why the three indexes (GCVI, NDVI, and PSRI) were chosen as the indicator of phenological periods were explained as follows:

First, in the leafless period of PaWs, there is no leaf on the PaWs but there are leaves on the evergreen trees. During this period, the soil signal may affect the vegetation reflectance significantly, making it difficult to detect the weak chlorophyll signal (Huete, 1988). While the GCVI can respond to lower chlorophyll levels, and the broad spectral band characteristics make it a high sensitivity and signal-to-noise ratio for chlorophyll content (Gitelson et al., 2003). Consequently, the GCVI was used as an indicator of the leafless period of PaWs to distinguish PaWs and the evergreen vegetation. Second, NDVI is chlorophyll sensitive and has been widely applied in the monitoring of photosynthetically active biomass of plant canopies (Huete et al., 2002; Tucker, 1979). In the greenleaf period of PaWs, the chlorophyll content is increasing. Therefore it is suitable for NDVI to monitor greenleaf period of PaWs. Finally, PSRI was chosen to indicate the senescence period, because in the senescence period, the leaves of PaWs turn yellow. PSRI can respond to pigment changes during this leaf senescence period.

Through the analysis of Fig. 4, three key phenological periods of PaWs: leafless period, greenleaf period, and senescence period can be identified as follows:

(1) Leafless period. During the leafless period, there is no leaf on the PaWs. The chlorophyll content of the PaWs is at the lowest level of a year, which resulted in the steady valley value of GCVI during DoY 0 to 65. During this time period, NDVI is also at the lowest level of a year. Consequently, the DoY of 0 to 65 was regarded as the leafless period.

(2) Greenleaf period. The leaves of PaWs are mature and with high canopy densities, the chlorophyll content of PaWs achieves the highest in a year. According to Fig. 4, the value of NDVI is at the maximum level while the value of PSRI is at the minimum level during DoY of 145 ~

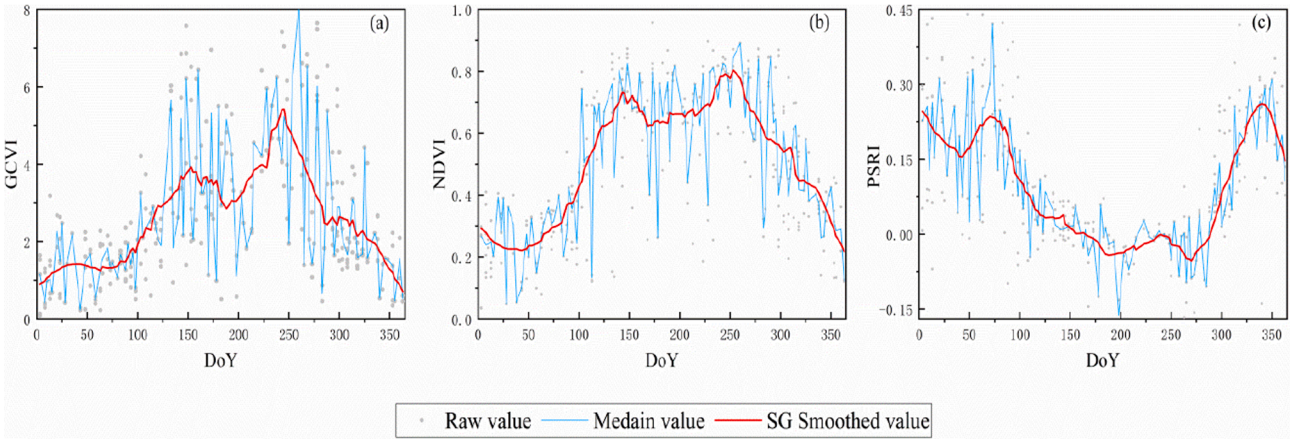

Fig. 4. (a), (b), and (c) represent the temporal profile of GCVI, NDVI, and PSRI, respectively.

255. Therefore, the DoY of 145 to 255 was taken as the greenleaf period.

(3) Senescence period. During the senescence period, the leaves of PaWs gradually turn yellow. Correspondingly, the senescence signature of PaWs increases progressively, and the chlorophyll content is gradually declining. During the DoY of 270 to 340, the value of PSRI increases while the NDVI value decreases steadily. Thus the DoY of 270 to 330 was defined as the senescence period.

3.1.3. Image composition

According to the identified three key phenological periods, a new feature was constructed by the three key phenological periods and the multi-scale RGB images. Five spectral vegetation indexes were taken to characterize the three phenological periods. The five indexes were GCVI, NDVI, Enhanced Vegetation Index (EVI) (Huete et al., 2002; Huete et al., 1997), Land Surface Water Index (LSWI) (Xiao et al., 2004), and PSRI (Table 1), respectively. All the spectral vegetation indexes data was derived from the Sentinel-2 SR images on the GEE platform. Among the five indexes, the GCVI was used in leafless period; NDVI, EVI, and LSWI were used in greenleaf period; PSRI was applied to the senescence period. The multi-scale RGB images were the sub-meter GE images and the 10 m Sentinel-2 RGB images acquired on GEE. For each vegetation index image acquired from the GEE platform, the median value pixel-based image composite method was used, specifically, each pixel of the vegetation index images was obtained by taking the median index value of all available pixels. Afterwards, all the index pixels were composited into a complete image. The reason why the five indexes were chosen for constructing the new feature was as follows: (1) GCVI, designed as an indicator of vegetation chlorophyll content, was sensitive to the appearance of green leaves. In this study, GCVI was used in the leafless period of PaWs to differentiate it from the evergreen vegetation. (2) NDVI is sensitive to vegetation growth, whereas it has been found that NDVI will gradually saturate when the biomass continues to elevate, especially in the greenleaf period of PaWs. By contrast the EVI will remain sensitive to the high biomass periods (Cai et al., 2018; Huete et al., 2002; Pastor-Guzman et al., 2018). Therefore, the NDVI and EVI were both used complementarily in the greenleaf period of PaWs. (3) The shortwave infrared (SWIR) band is crucial to the assessment of vegetation water content, and the NIR-SWIR vegetation indexes can respond to the change of the leaf water content (Brook et al., 2020; Ceccato et al., 2002; Yan et al., 2010). Consequently, the LSWI was taken as the indicator of the water content of vegetation (Xiao et al., 2002; Xiao et al., 2004). During the greenleaf period of PaWs, the leaf water content is at the highest level in a year and transpiration of PaWs may lead to the increase of water content in canopy. LSWI has the potential to monitor the changes of water content, and was thus selected during the greenleaf period. (4) In the senescence period, the leaves of PaWs turn yellow. PSRI can respond to pigment changes during the leaf senescence. Consequently, we employed the PSRI to characterize the senescence period of PaWs.

Table 1
The formulas of spectral indexes used in the phenological periods of PaWs.

Spectral index	Formulation	Phenological periods
GCVI	GCVI = NIR / Green −1	Leafless period
NDVI	NDVI = (NIR – Red) / (NIR + Red)	Greenleaf period
EVI	EVI = 2.5 × (NIR-Red) / (NIR + 6 × Red − 7.5 × Blue + 1)	Greenleaf period
LSWI	LSWI = (NIR - SWIR) / (NIR + SWIR)	Greenleaf period
PSRI	PSRI= (Red - Blue) / Red Edge 2	Senescence period

3.2. Evaluation of spectral separability

The classification accuracy depends on the inter-class spectral separability to a large extent (Kailath, 1967; Tolpekin and Stein, 2009). To evaluate the effectiveness of our proposed method (Spsf) in improving the spectral separability between PaWs and other tree species as well as reducing redundant information, comparative experiments were conducted on spectral separability between the Spsf images and other composite images. The multiple composite images were obtained through arranging and combining the different phenological images. All the composite images can be seen in Table 2. Considering the circumstances that the urban tree species are diverse and the surrounding species of PaWs are various and irregular, we divided the surrounding species of PaWs into evergreen and deciduous tree species. The Jeffries-Matusita (JM) distance, a widely applied spectral separability indicator, was employed to quantify the spectral separability between PaWs and the surrounding species. The value range of JM is 0 ~ 2, and the larger the JM values, the higher the spectral separability between classes, and vice versa (Schmidt and Skidmore, 2003). In this research, all the JM values were calculated by ENVI 5.3. Limited by the processing speed and image storage space of ENVI 5.3, two small areas of each composite image in the study area were selected to calculate the JM distance. The vegetation distribution between the two areas was different, and each small area covered roughly-one-tenth of the entire study area.

3.3. DL training and prediction

In addition to the composite feature, an effective classifier is of great importance to PaWs identification. Machine learning has been widely used in remote sensing image processing. As one of the branches of machine learning, DL has been demonstrated great potential in image classification over the past few years (Kussul et al., 2017; Liu et al., 2020). Compared to traditional machine learning, DL can learn the

Table 2
The composite images and their corresponding bands or indexes.

imagery	Corresponding bands / indexes	Expression
Basic image	GE RGB bands (GE RGB)	a
Basic image, Sentinel-2 image	GE RGB, S2 RGB	ab
Basic image, leafless	GE RGB, GCVI	ac
Basic image, greenleaf	GE RGB, NDVI, EVI, LSWI	ad
Basic image, senescence	GE RGB, PSRI	ae
Basic image, Sentinel-2 image, leafless	GE RGB, S2 RGB, GCVI	abc
Basic image, Sentinel-2 image, greenleaf	GE RGB, S2 RGB, NDVI, EVI, LSWI	abd
Basic image, Sentinel-2 image, senescence	GE RGB, S2 RGB, PSRI	abe
Basic image, Sentinel-2 image, leafless, greenleaf	GE RGB, S2 RGB, GCVI, NDVI, EVI, LSWI	abcd
Basic image, Sentinel-2 image, leafless, senescence	GE RGB, S2 RGB, GCVI, PSRI	abce
Basic image, Sentinel-2 image, greenleaf, senescence	GE RGB, S2 RGB, NDVI, EVI, LSWI, PSRI	abde
Basic image, leafless, greenleaf	GE RGB, GCVI, NDVI, EVI, LSWI	acd
Basic image, leafless, senescence	GE RGB, GCVI, PSRI	ace
Basic image, greenleaf, senescence	GE RGB, NDVI, EVI, LSWI, PSRI	ade
Basic image, leafless, greenleaf, senescence	GE RGB, GCVI, NDVI, EVI, LSWI, PSRI	acde
Sentinel-2 image, leafless, greenleaf, senescence	S2 RGB, GCVI, NDVI, EVI, LSWI, PSRI	bcde
Basic image, Sentinel-2 image, leafless, greenleaf, senescence	GE RGB, S2 RGB, GCVI, NDVI, EVI, LSWI, PSRI	abcde

context surrounding the object of interest and take the relationship among pixels into account (Korznikov et al., 2021). Semantic segmentation is one of the fundamental topics in computer vision, and a multitude of DL models have been developed for semantic segmentation. To our knowledge, DeepLabv3+, as the state-of-the-art version of DeepLabv3, plays an important role in simplifying the interpretation of remote sensing images (Sun and Wang, 2018). In this study, DeepLabv3 + was taken as the semantic segmentation model for DL training. Meanwhile, the DenseNet convolutional neural network (CNN) was chosen as the backbone network of DeepLabv3 + in this research. There were several remarkable merits of DenseNet. For example, through the DenseNet backbone, the problem of vanishing gradient can be alleviated. The features can be transferred and reused more effectively, and the number of parameters can be reduced significantly. Moreover, the flow of information and gradients can be improved, which makes the training more easily (Huang et al., 2017; Wang and Chang, 2019). Consequently, referring to the study of (Wang and Chang, 2019), the DenseNet-121 version was applied in the DeepLabv3 + model.

The Windows 10 machine, equipped with the GPU of RTX 3090 and 24 GB memory, was used for DL training and prediction with the TensorFlow framework. The initial learning rate was set to be 0.001, and the training batch size was 10, and the training number of epochs was set to be 1000. The MeanIoU and loss were taken as the indicators to evaluate the trained models and the model with the maximum MeanIoU and the minimum loss was considered as the optimal prediction model. The code used in this study for semantic segmentation and details about the configuration of DeepLabv3 + model training and prediction were referenced the https://github.com/TachibanaYoshino/Remote-sensing-image-semantic-segmentation-tf2.

4. Results

4.1. Evaluation of spectral separability

In order to evaluate the effectiveness of Spsf in improving spectral separability between PaWs and other tree species, the JM values were calculated using all the composite images. Fig. 5 showed the JM values between PaWs and other deciduous (or evergreen) tree species for 15 types of composite images. For the spectral separability between PaWs and evergreen trees, the basic GE RGB imagery (a) got the consistently minimum JM values (range from 0.12 to 0.48) in two areas. In contrast, the maximum JM values (range from 1.77 to 1.89) were achieved by the Spsf-based image (abcde), and followed by the combination of basic image and leafless period, greenleaf period, and Sentinel-2 RGB image (abcd), ranging from 1.70 to 1.86. Meanwhile, we found that the leafless period contributed the most to the improvement of the JM values between PaWs and evergreen tree species (from 0.12 to 1.09 and from 0.48 to 1.45) when adding the images of a single phenological period to the basic GE RGB image. As regards the spectral separability between PaWs and other deciduous tree species, the basic GE RGB image (a) got the minimum JM value (1.20 and 0.87) similarly. The Spsf-based image (abcde) achieved the maximum JM values (1.71 and 1.65), followed by the combination of basic image and leafless period, greenleaf period, and Sentinel-2 RGB image (abcd), with a range from 1.69 to 1.57. The results showed that the spectral separability between PaWs and other deciduous (or evergreen) vegetation was the lowest based on the GE submeter image. And the spectral separability increased with the incorporation of the phenological features. Finally, the Spsf-based method reached the highest spectral separability, which meant that the Spsf-based method help greatly in the improvement of classification

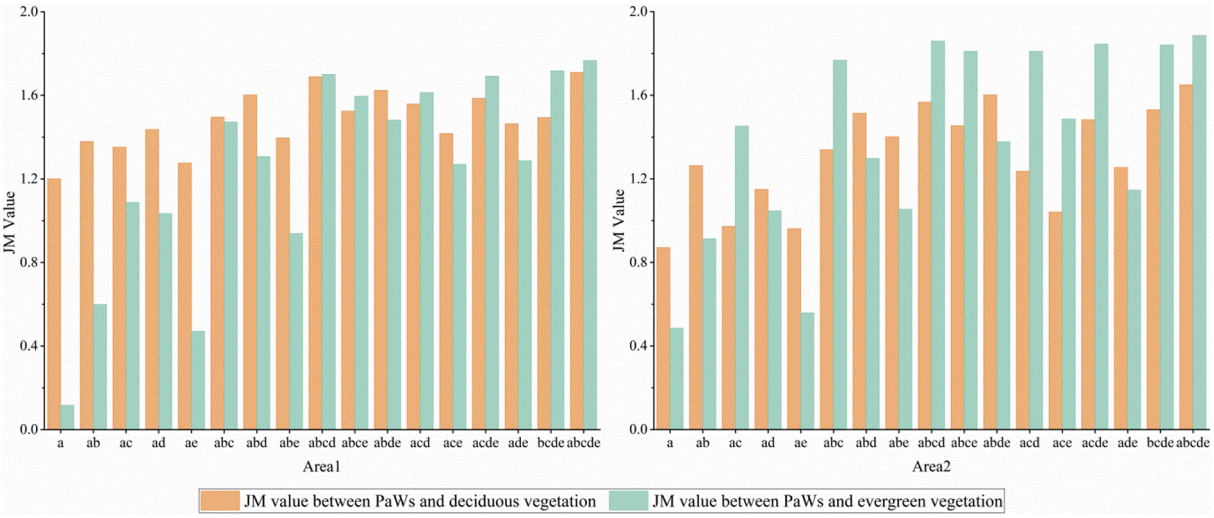

Fig. 5. The JM value results of 15 composite images in area1 and area2.

accuracy. Furthermore, we found that when only single period was incorporated in the basic GE image, the greenleaf period was the most effective in enhancing the spectral separability between PaWs and other deciduous trees (JM value from 1.19 to 1.44 and from 0.87 to 1.15), and the senescence period helped most in enhancing the spectral separability between PaWs and evergreen trees (JM value from 0.12 to 1.09 and from 0.48 to 1.45).

As a whole, the Spsf-based method achieved the maximum JM value between PaWs and other tree species. Therefore, in this research, it is more appropriate to combine the three phenological periods, the basic GE imagery and Sentinel-2 SR imagery.

4.2. Classification accuracy

With the optimal composite image (Spsf), the DeepLabv3 + semantic segmentation model was employed for training, and the DenseNet-121 was taken as the classification CNN. After the 1000 training epochs, we obtained the optimal model with MeanIoU of 0.95 and loss of 0.015. The Spsf map was then acquired through the optimal model. The accuracy of the Spsf map was assessed using the field survey data acquired in 2020. As shown in Table 3. The Spsf achieved the overall accuracy (OA) of about 91 %, and the Kappa coefficient of 0.83. The producer accuracy (PA) and the user accuracy (UA) of PaWs were 90.45 % and 95.27 %, respectively. Some details about the prediction results can be seen in Fig. 6. We found that the DL prediction results can match the validation labels well. For the first row, despite the fragmented distribution and small size of PaWs on both sides of the road, those PaWs areas can be accurately predicted by the proposed Spsf-based DL model. Similarly, discrete PaWs distributed in the park can be accurately classified in the third row. As for the second row, the PaWs are densely distributed and large in size, and the DL prediction results are highly accurate compared with the validation samples. Meanwhile, the small intervals between the PaWs can be identified. The complete prediction results of PaWs can be found in the following GEE application URL: https://2200902201.users.earthengine.app/view/spsf.

Despite promising results achieved, there still existed some omissions and commissions possibly due to the following reasons. First, we acquired the GE RGB image from 2019 ~ 2020, while the field survey data was acquired in 2020. The changes of land cover types may result in the errors in the classification results. Second, some shadows were misclassified as PaWs. Third, although the partitioning method was used to acquire the GE RGB image, the image quality of some areas were still not satisfactory, possibly leading to the poor prediction results for these areas. More analysis about the uncertainty of the prediction results will be shown in the discussion section (Section 5.2).

The phenological features can improve the classification accuracy by augmenting the spectral separability between PaWs and others. The effectiveness can be quantified by JM values while the effect of the rich spatial information contained by GE imagery cannot be assessed with this measure. Although the VHR GE imagery was rarely taken as a single data source for classification, the rich spatial information was useful for improving the accuracy of urban tree species detection (Dong et al., 2019). Therefore, comparative experiments were performed to demonstrate the irreplaceable effect of GE imagery on optimizing classification results. To ensure a reasonable comparison, we set the same parameters for the GE RGB band removed image as those for the Spsf-based image when training the DL model. Finally, we acquired the MeanIoU of 0.89 and loss of 0.021. Thereafter, 890 PaWs field survey sample points and 610 non-PaWs sample points were utilized for accuracy validation on the PaWs map derived from the optimal prediction model. As shown in Table 4, the final prediction results reached an overall accuracy of 0.87 and the Kappa coefficient of 0.74. The detailed comparison results can be found in Fig. 7. Columns a, and e represent the GE sub-meter image and the Sentinel-2 image resampled to 0.8 m resolution, respectively. We found that ground objects can be presented clearly by the GE sub-meter image while the Sentinel-2 image cannot delineate the boundary of ground objects precisely. Compared with the Spsf-based method, the OA decreased approximately by 5 % based on the image with GE RGB bands removed. Although the OA only slightly decreased, we found that the PA and UA of PaWs decreased largely (dropped from 90.45 % to 78.20 % and from 95.27 % to 75.69 %). The prediction results of the GE RGB band removed image had significant omission errors (see the row a, and b of the fourth column) and commission errors (see the row c of the fourth), and there were only 696 of 840 PaWs sample points correctly classified. The comparison results indicated the irreplaceable role of GE sub-meter images for accurate tree species classification.

Table 3
Accuracy assessment of the Spsf-based PaWs map.

Class	Ground truth samples		PA (%)	UA (%)	OA (%)	Kappa
	PaWs	Non-PaWs				
PaWs	805	85	90.45	95.27	91.67	0.83
Non-PaWs	40	570	93.44	87.02		

4.3. Uncertainty analysis

Although the good results from the Spsf method, there are still several uncertainty factors that may affect the final mapping results. The classification accuracy depends on the inter-class spectral separability to a large extent (Kailath, 1967; Tolpekin and Stein, 2009). And the JM distance, as a spectral separability indicator, has been widely used to quantify the spectral separability in land cover classification (Ni et al., 2021; Tian et al., 2020). The value range of JM is 0 ~ 2, and the larger the JM values, the higher the spectral separability between classes, and vice versa (Schmidt and Skidmore, 2003). Therefore, the JM values were taken to quantify the uncertainties in the Spsf method. And the uncertainty analysis mainly includes two aspects: (1) sub-meter GE RGB imagery; (2) phenological spectral features. First, the sub-meter GE RGB imagery not only enriched the spectral information, but also provided rich spatial information for the Spsf feature. The improvement of the spectral separability by GE imagery is quantified by the JM values, and the function of the spatial information was reflected by the final mapping accuracy. As for the JM values (Fig. 5), we compared the results of the Spsf image (abcde) and the GE RGB band removed image (bcde). We found that the spectral separability was enhanced when the GE imagery was incorporated, and the JM values between PaWs and the deciduous vegetation (from 1.49 to 1.70 and from 1.53 to 1.64) increased more significantly than the values between PaWs and the evergreen vegetation (from 1.72 to 1.77, and from 1.84 to 1.87). That may relate to the acquisition time of GE imagery, the summer imagery may be more effective in distinguishing PaWs from deciduous vegetation. Furthermore, the accuracy of the prediction results for Spsf image and the GE RGB band removed image were compared. When the GE imagery was removed, the omission errors and commission errors increased significantly. The OA decreased from 91.67 % to 86.67 % and Kappa decreased from 0.83 to 0.74, which has shown the indispensable role of spatial information from GE imagery in improving the mapping accuracy. Second, the phenological spectral features in Spsf method were derived from the three key phenological periods. The JM values represented the contribution of each phenological period to the final mapping accuracy. Phenological spectral features from the composition of three key phenological periods achieved the highest JM values (abcde), and the JM values decreased with the reduction of phenological spectral features. And we found that the spectral separability between PaWs and the deciduous vegetation was most significantly reduced when the greenleaf period feature was removed (from 1.71 to 1.52 and from 1.65 to 1.45), and when the leafless period feature was removed, the spectral separability between PaWs and the evergreen vegetation decreased the most (from 1.77 to 1.48 and from 1.89 to 1.38). The above showed that the three key phenological periods contributed unequally in enhancing the

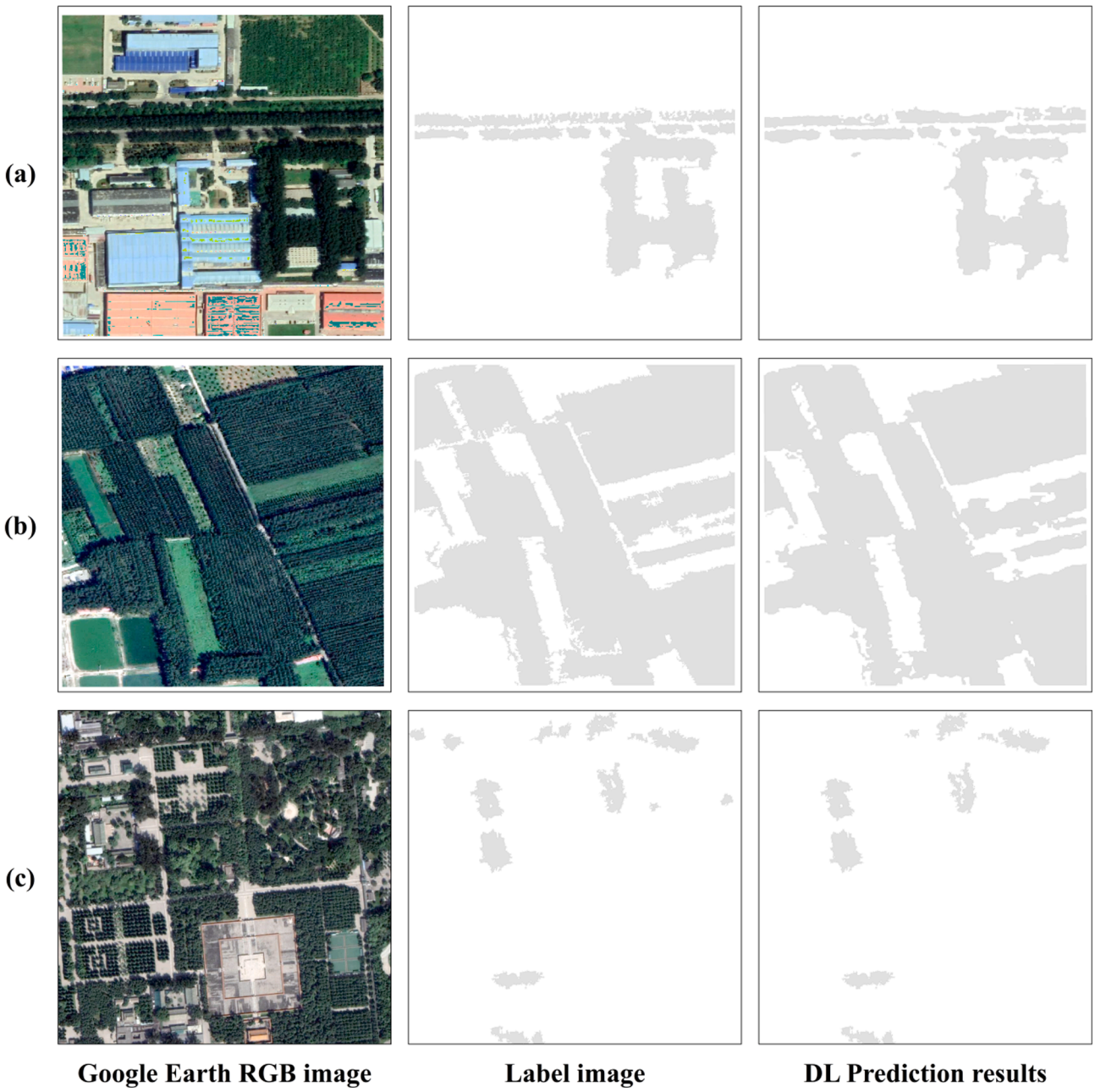

Fig. 6. Comparisons of some details about the label images and the corresponding DL prediction results. The first column represents the GE RGB image; the second column indicates the label image used for validation; the third column is the DL prediction results of Spsf. The a, b, and c represent three different growth scenes of PaWs growth, respectively. Row a represents the densely small area of PaWs along the road, row b is the densely large area of PaWs, and row c indicates the fragmented small area PaWs in the park.

Table 4
Accuracy assessment of the PaWs map derived from the images without the GE RGB bands.

Class	Ground truth samples		PA (%)	UA (%)	OA (%)	Kappa
	PaWs	Non-PaWs				
PaWs	696	194	78.20	75.69	86.67	0.74
Non-PaWs	6	604	99.02	99.15		

spectral separability, the leafless period is the most effective in enhancing the spectral separability between PaWs and the evergreen vegetation, and the greenleaf period helped most to distinguish PaWs and the deciduous vegetation.

5. Discussion

5.1. The advantages of the Spsf method

Constructing the urban tree species mapping has been a challenge for a long time due to two constraints: (1) the complex composition and severe fragmentation of urban tree landscapes, which may result in the existence of mixed pixels; (2) the tree species in urban environment are diverse with high spectral similarity. The sub-meter GE remote sensing images can not only solve the issue of mixed pixels caused by coarse resolution images (Du et al., 2017), but also are less constrained by cost, time, and space. Utilizing the phenological features has been considered to be effective to enhance the spectral separability (Fang et al., 2020; Zeng et al., 2020). Consequently, a sub-meter phenological spectral

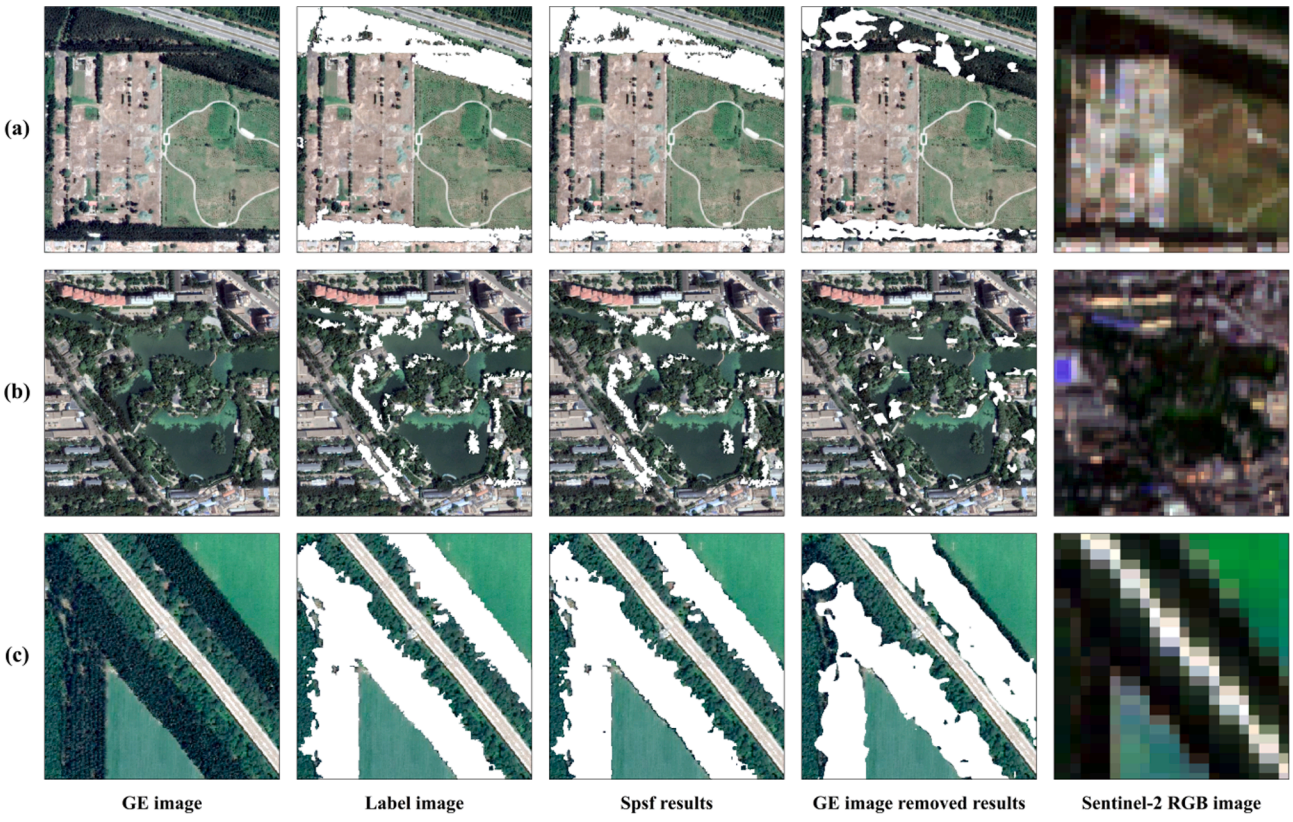

Fig. 7. Some detailed Comparisons between the Label images, Spsf prediction results, and the prediction results of GE RGB band removed image. The first column is GE image; the second column represents the reference label image; the third column indicates the prediction results of Spsf-based image; the fourth column features the prediction results of image with GE RGB bands removed from Spsf; the fifth column shows the Sentinel-2 RGB image which was resampled to 0.8 m resolution. The rows a and b of the fourth column present the omission errors of PaWs, and the row c of the fourth column presents the commission errors of PaWs.

feature (Spsf) was developed to conduct the accurate mapping of PaWs in the urban area (the Beijing Plain). The promising results of Spsf may attribute to two aspects: (1) Spsf explored three key phenological periods of PaWs and characterized them through five spectral vegetation indexes, which largely help enhance the spectral separability between PaWs and others; (2) Spsf made the utmost of the spatial information of free sub-meter GE imagery and the spectral-phenological information of Sentinel-2 SR imagery, which can minimize the occurrence of mixed pixels.

5.1.1. The importance of three key phenological periods

Three key phenological periods specific to the PaWs were incorporated to augment the spectral separability between PaWs and others. Those periods can help distinguish tree species with different phenological patterns to improve the mapping accuracy (Diao and Wang, 2016). In the leafless period, there is no leaf on the deciduous trees, but there are leaves on the evergreen trees. Although the spectral characteristics during this period cannot be leveraged to differentiate PaWs from other deciduous trees, they can be used effectively to distinguish PaWs from the evergreen trees. In the greenleaf period, the leaves of PaWs are gradually mature with high canopy densities. Because of the high transpiration of PaWs (Guidi et al., 2008; Isebrands and Richardson, 2014), the moisture level on the surface of PaWs is higher than other deciduous trees, which can be taken as a feature to distinguish PaWs from others. In the senescence period, the leaves of PaWs are gradually turning yellow. Because the poplars have a long growing period with extended coloration, in the senescence periods of PaWs, the leaves of most other deciduous trees have already withered while the leaves of evergreen trees are still green. Therefore, the spectral separability among PaWs, other deciduous tree species, and evergreen tree species can be enhanced in the senescence period.

In addition to the three key phenological periods, it is also important to select appropriate spectral vegetation indexes to characterize the key phenological periods to enhance the spectral separability between PaWs and other trees (Inoue et al., 2020; Ni et al., 2021; Zhang et al., 2020). In this research, five spectral indexes (i.e. GCVI, NDVI, EVI, LSWI, and PSRI) were applied to characterize the three phenological periods of PaWs for the first time. The JM values (see Section 4.1) indicated the great potential of spectral indexes in augmenting the spectral separability between PaWs and others. The GCVI, sensitive to the change of chlorophyll and leaf area, was taken to characterize the leafless period in which the difference between PaWs and evergreen trees can be reflected in the chlorophyll content. The NDVI, EVI, and LSWI were selected to characterize the greenleaf period because of their demonstrated performance in the identification of the chlorophyll signal and leaf water content. In the greenleaf period, the chlorophyll and water content are at the peak of a year. Despite the sensitivity of NDVI to chlorophyll content, it tends to saturate gradually in the high biomass regions which may limit the accuracy of detection results. Alternatively, EVI can sensitively capture the variations of vegetation canopy structures of high biomass regions which may complement NDVI in tree species detection (Cai et al., 2018; Huete et al., 2002; Pastor-Guzman et al., 2018). LSWI is water sensitive and is developed to estimate the canopy moisture thickness (Cai et al., 2018). Because of the high transpiration of PaWs, LSWI was used as an indicator to quantify the leaf water content difference between PaWs and other trees. Therefore, the NDVI, EVI, and LSWI were chosen for characterizing PaWs during the greenleaf period. In the senescence period, the leaves of PaWs are gradually turning yellow. PSRI was employed in the senescence period because it is more responsive to the pigment changes caused by the senescence than other indexes (Merzlyak et al., 1999).

5.1.2. The benefits of GE sub-meter RGB imagery

GE imagery had been proved to be of great potential in object detection (Guo et al., 2016; Hu et al., 2013). Through the sub-meter GE imagery, we can acquire rich spatial information and solve the issue of mixed pixels in remote sensing imagery of relatively coarse spatial resolutions (Delrue et al., 2013; Dixit and Agarwal, 2020; Du et al., 2017). In this study, sub-meter GE imagery was used as a component of Spsf to improve the PaWs mapping accuracy. To demonstrate the indispensable role of GE imagery in accurate PaWs mapping, comparative experiments were carried out between the Spsf-based image and the GE RGB band removed image (as seen in Fig. 7). Columns a, and e of Fig. 7 represent the GE sub-meter image and the Sentinel-2 image that were resampled to 0.8 m resolution, respectively. We found that the prediction results of Spsf-based image match well with the actual distribution of PaWs and the details of the boundary can be captured with high accuracy, while the prediction results of the GE RGB band removed image cannot represent the real PaWs distribution accurately. There are also significant omission errors (see the row a, and b in the fourth column) and commission errors (see the row c in the fourth column) using the GE RGB band removed image. This comparative analysis indicated that the GE RGB imagery contains abundant land surface information and possesses rich spatial characteristics of image objects such as shape and texture (Li et al., 2012; Marcos et al., 2018), which can help retain the boundary information more completely (Wen et al., 2021). Additionally, contextual information is a dominant feature in VHR images (Mura et al., 2008), and the CNN-based DL training method can learn the context surrounding the object of interest and take the relationship between pixels into account. The powerful self-learning capability of CNN enables it to analyze the texture features of images efficiently and extract those features automatically which are important for image classification. The extracted features can help to detect the spatial variations in brightness and intensity of local areas (Li et al., 2020), which is useful for identifying the leaf and canopy information of PaWs (Wang et al., 2016; Zhang et al., 2018).

5.2. The implications of PaWs map and future work

This study conducted the sub-meter accurate mapping of PaWs in the Beijing Plain. As shown in Section 4.2, the Spsf achieved high accuracy and the derived sub-meter PaWs map can be considered a notable innovation in urban tree species identification. The PaWs map can further facilitate the environmental management of the Beijing Plain to improve the residents' health level. The Beijing Plain is densely populated and the PaWs are widely planted. When people are exposed to the PWCs, allergic reactions and respiratory diseases are more likely to be triggered. It is crucial to carry out accurate monitoring and management of PaWs. The traditional manual measurement method to detect PaWs is time-consuming and labor-intensive. The fragmented distribution of PaWs in urban environment, along with the high spectral similarity between tree species, also make it difficult for the coarse-resolution remote sensing images to achieve accurate tree species identification. Despite the potential of high-resolution images, the acquisition cost associated with those images hinders the monitoring of PaWs at large scales. The Spsf provided a new paradigm for dealing with the above issues. What's more, for other areas encountering the disturbance from PWCs, the Spsf-based method can provide a new perspective for urban PaWs monitoring and management so that the relevant departments can take proactive strategies during the seasons of PWCs to minimize the pollution of the urban environment and the harm to human health.

Although the Spsf map has achieved high accuracy, there are still some limitations with this study. First, the GE imagery was obtained from different data sensors, so the image may subject to color deviation and inconsistent color tone. The color consistency processing was thereby worth trying to mitigate these problems. Second, all the Sentinel-2 images were acquired through the median composite method on the GEE to remove the extreme values caused by clouds and cloud shadows (Azzari and Lobell, 2017; Bey et al., 2020; Jin et al., 2019). However, the median composite method cannot highlight the peak of the data which may be beneficial to the phenological features. Other image composite methods could thus be further explored in future studies. Third, Spsf was developed by simply stacking the spatial feature of sub-meter GE imagery and the phenological feature of Sentinel-2 imagery. The spatiotemporal fusion of remote sensing imagery may take advantage of complementary observations of multi-source data and mine for more potential information to enhance target characteristics (Shi et al., 2022). Therefore, it is worthwhile to try the feature fusion methods for Spsf. Fourth, there were still some shadows misclassified as PaWs in the Spsf map, so a shadow removal algorithm could be incorporated in future studies to improve the mapping accuracy. Fifth, although good results for PaWs mapping have been yielded in the Beijing plain through the Spsf-based method, there may be differences in the phenological periods of PaWs in other regions due to the difference in climate and surrounding environment. Therefore, more factors should be taken into account in the Spsf-based method to develop a more generalizable PaWs detection model. Sixth, when there is a lack of a certain phenological image, we can use images from adjacent years to make up for it, or only use the remaining phenological images to achieve relatively good results. Seventh, this study has captured the three key phenological periods of PaWs in Beijing Plain, but when applying the phenological periods to other tree species, it may lead to poor results because different tree species may vary greatly in phenological periods (Grillakis et al., 2022; Zhou et al., 2016). Consequently, when mapping other tree species, it is necessary to analyze the specific phenological periods according to local conditions (e.g. climate) based on the Spsf method.

6. Conclusion

This study developed a sub-meter phenological spectral feature (Spsf) for mapping the distribution of PaWs on a regional scale by incorporating the freely sub-meter GE image and phenological features. The spectral separability between PaWs and other tree species was improved largely, which can be attributed to the fact that Spsf carries rich phenological spectral information over the whole growing period of PaWs as well as extensive spatial landscape information of PaWs. We found that the leafless period was the most effective in enhancing the spectral separability between PaWs and evergreen trees. The greenleaf period helped the most in distinguishing the PaWs from deciduous trees. Finally, we obtained the sub-meter PaWs distribution map in the Beijing Plain using the advanced DL model with high accuracy. The Spsf-based method facilitates the shaping of a new paradigm for sub-meter accurate mapping of urban tree species. The derived PaWs map can provide basic reference data for the relevant departments to monitor and manage the PWCs.

Declaration of Competing Interest

The authors declare that they have no known competing financial interests or personal relationships that could have appeared to influence the work reported in this paper.

Acknowledgments

We sincerely thank the anonymous reviewers for their insightful comments and suggestions. We also sincerely thank Dr. Junfei Xie and Piesat Information Technology Co., Ltd. for the data support. This work is supported by the National Natural Science Foundation of China (No. 42171330) and the Beijing Outstanding Young Scientist Program (No. BJJWZYJH01201910028032).

Appendix A. Supplementary data

Supplementary data to this article can be found online at https://doi.org/10.1016/j.isprsjprs.2022.09.002.

References

Azzari, G., Lobell, D.B., 2017. Landsat-based classification in the cloud: An opportunity for a paradigm shift in land cover monitoring. Remote Sens. Environ. 202, 64–74.

Berni, J.A.J., Zarco-Tejada, P.J., Suarez, L., Fereres, E., 2009. Thermal and Narrowband Multispectral Remote Sensing for Vegetation Monitoring From an Unmanned Aerial Vehicle. IEEE Trans. Geosci. Remote Sens. 47, 722–738.

Bey, A., Jetimane, J., Lisboa, S.N., Ribeiro, N., Sitoe, A., Meyfroidt, P., 2020. Mapping smallholder and large-scale cropland dynamics with a flexible classification system and pixel-based composites in an emerging frontier of Mozambique. Remote Sens, Environ, p. 239.

Brook, A., De Micco, V., Battipaglia, G., Erbaggio, A., Ludeno, G., Catapano, I., Bonfante, A., 2020. A smart multiple spatial and temporal resolution system to support precision agriculture from satellite images: Proof of concept on Aglianico vineyard. Remote Sens, Environ, p. 240.

Cai, Y., Guan, K., Peng, J., Wang, S., Seifert, C., Wardlow, B., Li, Z., 2018. A high-performance and in-season classification system of field-level crop types using time-series Landsat data and a machine learning approach. Remote Sens. Environ. 210, 35–47.

Ceccato, P., Gobron, N., Flasse, S., Pinty, B., Tarantola, S., 2002. Designing a spectral index to estimate vegetation water content from remote sensing data: Part 1 - Theoretical approach. Remote Sens. Environ. 82, 188–197.

Chen, K., Fu, K., Yan, M., Gao, X., Sun, X., Wei, X., 2018. Semantic Segmentation of Aerial Images With Shuffling Convolutional Neural Networks. IEEE Geosci. Remote Sens. Lett. 15, 173–177.

Chen, J., Jonsson, P., Tamura, M., Gu, Z.H., Matsushita, B., Eklundh, L., 2004. A simple method for reconstructing a high-quality NDVI time-series data set based on the Savitzky-Golay filter. Remote Sens. Environ. 91, 332–344.

de Castro, A.I., Six, J., Plant, R.E., Pena, J.M., 2018. Mapping Crop Calendar Events and Phenology-Related Metrics at the Parcel Level by Object-Based Image Analysis (OBIA) of MODIS-NDVI Time-Series: A Case Study in Central California. Remote Sensing 10.

Delrue, J., Bydekerke, L., Eerens, H., Gilliams, S., Piccard, I., Swinnen, E., 2013. Crop mapping in countries with small-scale farming: a case study for West Shewa, Ethiopia. Int. J. Remote Sens. 34, 2566–2582.

Diao, C.Y., Wang, L., 2016. Incorporating plant phenological trajectory in exotic saltcedar detection with monthly time series of Landsat imagery. Remote Sens. Environ. 182, 60–71.

Dixit, A., Agarwal, S., 2020. Super-resolution mapping of hyperspectral data using Artificial Neural Network and wavelet. Remote Sensing Applications-Society and Environment 20.

Dong, T., Shen, Y., Zhang, J., Ye, Y., Fan, J., 2019. Progressive Cascaded Convolutional Neural Networks for Single Tree Detection with Google Earth Imagery. Remote Sensing 11.

Dorren, L.K.A., Maier, B., Seijmonsbergen, A.C., 2003. Improved Landsat-based forest mapping in steep mountainous terrain using object-based classification. For. Ecol. Manage. 183, 31–46.

Du, Z., Zhang, Y., Zhang, F., Liu, R., Chen, Y., 2017. Multiple endmember object spectral mixture analysis for high spatial resolution remote sensing imagery of urban areas. J. Appl. Remote Sens. 11.

eCognition Developer, T., 2014. 9.0 User Guide. Trimble Germany GmbH: Munich, Germany.

Evangelista, P.H., Stohlgren, T.J., Morisette, J.T., Kumar, S., 2009. Mapping invasive tamarisk (Tamarix): a comparison of single-scene and time-series analyses of remotely sensed data. Remote Sensing 1, 519–533.

Fang, F., McNeil, B.E., Warner, T.A., Maxwell, A.E., 2018. Combining high spatial resolution multi-temporal satellite data with leaf-on LiDAR to enhance tree species discrimination at the crown level. Int. J. Remote Sens. 39, 9054–9072.

Fang, F., McNeil, B.E., Warner, T.A., Maxwell, A.E., Dahle, G.A., Eutsler, E., Li, J.L., 2020. Discriminating tree species at different taxonomic levels using multi-temporal WorldView-3 imagery in Washington DC. USA. Remote Sens, Environ, p. 246.

Fassnacht, F.E., Latifi, H., Sterenczak, K., Modzelewska, A., Lefsky, M., Waser, L.T., Straub, C., Ghosh, A., 2016. Review of studies on tree species classification from remotely sensed data. Remote Sens. Environ. 186, 64–87.

Felix, E., Tilley, D.R., Felton, G., Flamino, E., 2008. Biomass production of hybrid poplar (Populus sp.) grown on deep-trenched municipal biosolids. Ecol. Eng. 33, 8–14.

Geng, R., Jin, S., Fu, B., Wang, B., 2020. Object-Based Wetland Classification Using Multi-Feature Combination of Ultra-High Spatial Resolution Multispectral Images. Canadian Journal of Remote Sensing 46, 784–802.

Gitelson, A.A., Gritz, Y., Merzlyak, M.N., 2003. Relationships between leaf chlorophyll content and spectral reflectance and algorithms for non-destructive chlorophyll assessment in higher plant leaves. J. Plant Physiol. 160, 271–282.

Gordon, J.C., 2001. Poplars: Trees of the people, trees of the future. For. Chron. 77, 217–219.

Grabska, E., Hostert, P., Pflugmacher, D., Ostapowicz, K., 2019. Forest Stand Species Mapping Using the Sentinel-2 Time Series. Remote Sensing 11.

Grillakis, M.G., Doupis, G., Kapetanakis, E., Goumenaki, E., 2022. Future shifts in the phenology of table grapes on Crete under a warming climate. Agricultural and Forest Meteorology 318.

Guidi, W., Piccioni, E., Bonari, E., 2008. Evapotranspiration and crop coefficient of poplar and willow short-rotation coppice used as vegetation filter. Bioresour. Technol. 99, 4832–4840.

Guirado, E., Tabik, S., Alcaraz-Segura, D., Cabello, J., Herrera, F., 2017. Deep-learning Versus OBIA for Scattered Shrub Detection with Google Earth Imagery: Ziziphus lotus as Case Study. Remote Sensing 9.

Guo, Z., Shao, X., Xu, Y., Miyazaki, H., Ohira, W., Shibasaki, R., 2016. Identification of village building via Google Earth images and supervised machine learning methods. Remote Sensing 8, 271.

Hamrouni, Y., Paillassa, E., Cheret, V., Monteil, C., Sheeren, D., 2021. From local to global: A transfer learning based approach for mapping poplar plantations at national scale using Sentinel-2. ISPRS J. Photogramm. Remote Sens. 171, 76–100.

Hermosilla, T., Wulder, M.A., White, J.C., Coops, N.C., Hobart, G.W., Campbell, L.B., 2016. Mass data processing of time series Landsat imagery: pixels to data products for forest monitoring. Int. J. Digital Earth 9, 1035–1054.

Hu, Q., Wu, W., Xia, T., Yu, Q., Yang, P., Li, Z., Song, Q., 2013. Exploring the use of Google Earth imagery and object-based methods in land use/cover mapping. Remote Sensing 5, 6026–6042.

Huang, G., Liu, Z., Van Der Maaten, L., Weinberger, K.Q., 2017. Densely connected convolutional networks. In: Proceedings of the IEEE Conference on Computer Vision and Pattern Recognition, pp. 4700–4708.

Huete, A.R., 1988. A SOIL-ADJUSTED VEGETATION INDEX (SAVI). Remote Sens. Environ. 25, 295–309.

Huete, A., Didan, K., Miura, T., Rodriguez, E.P., Gao, X., Ferreira, L.G., 2002. Overview of the radiometric and biophysical performance of the MODIS vegetation indices. Remote Sens. Environ. 83, 195–213.

Huete, A.R., Liu, H.Q., Batchily, K., vanLeeuwen, W., 1997. A comparison of vegetation indices global set of TM images for EOS-MODIS. Remote Sens. Environ. 59, 440–451.

Inoue, S., Ito, A., Yonezawa, C., 2020. Mapping Paddy Fields in Japan by Using a Sentinel-1 SAR Time Series Supplemented by Sentinel-2 Images on Google Earth Engine. Remote Sensing 12.

Isebrands, J.G., Richardson, J., 2014. Poplars and willows: trees for society and the environment. CABI.

Ji, W., Wang, L., 2016. Phenology-guided saltcedar (Tamarix spp.) mapping using Landsat TM images in western US. Remote Sens. Environ. 173, 29–38.

Jia, K., Liang, S., Gu, X., Baret, F., Wei, X., Wang, X., Yao, Y., Yang, L., Li, Y., 2016. Fractional vegetation cover estimation algorithm for Chinese GF-1 wide field view data. Remote Sens. Environ. 177, 184–191.

Jin, Z., Azzari, G., You, C., Di Tommaso, S., Aston, S., Burke, M., Lobell, D.B., 2019. Smallholder maize area and yield mapping at national scales with Google Earth Engine. Remote Sens. Environ. 228, 115–128.

Johnson, B., Xie, Z.X., 2011. Unsupervised image segmentation evaluation and refinement using a multi-scale approach. ISPRS J. Photogramm. Remote Sens. 66, 473–483.

Kailath, T., 1967. The divergence and Bhattacharyya distance measures in signal selection. IEEE transactions on communication technology 15, 52–60.

Kollert, A., Bremer, M., Loew, M., Rutzinger, M., 2021. Exploring the potential of land surface phenology and seasonal cloud free composites of one year of Sentinel-2 imagery for tree species mapping in a mountainous region. Int. J. Appl. Earth Obs. Geoinf. 94.

Korznikov, K.A., Kislov, D.E., Altman, J., Dolezal, J., Vozmishcheva, A.S., Krestov, P.V., 2021. Using U-Net-Like Deep Convolutional Neural Networks for Precise Tree Recognition in Very High Resolution RGB (Red, Green, Blue) Satellite Images. Forests 12.

Kulawardhana, R.W., Popescu, S.C., Feagin, R.A., 2014. Fusion of lidar and multispectral data to quantify salt marsh carbon stocks. Remote Sens. Environ. 154, 345–357.

Kussul, N., Lavreniuk, M., Skakun, S., Shelestov, A., 2017. Deep Learning Classification of Land Cover and Crop Types Using Remote Sensing Data. IEEE Geosci. Remote Sens. Lett. 14, 778–782.

Li, H., Han, Y., Chen, J., 2020. Combination of Google Earth imagery and Sentinel-2 data for mangrove species mapping. J. Appl. Remote Sens. 14.

Li, H., Shi, Q., Wan, Y., Shi, H., Imin, B., 2021. Using Sentinel-2 Images to Map the Populus euphratica Distribution Based on the Spectral Difference Acquired at the Key Phenological Stage. Forests 12, 147.

Li, D., Tong, Q., Li, R., Gong, J., Zhang, L., 2012. Current issues in high-resolution earth observation technology. Science China-Earth Sciences 55, 1043–1051.

Li, Y., Wang, G., Wei, T., Fan, Z., Yan, P., 2016. Nitrogen and sulfur co-doped porous carbon nanosheets derived from willow catkin for supercapacitors. Nano Energy 19, 165–175.

Liu, W., Yue, A., Ji, J., Shi, W., Deng, R., Liang, Y., Xiong, L., 2020. Urban green space extraction from GF-2 remote sensing image based on DeepLabv3+ semantic segmentation model. Remote Sensing for Land & Resources 32, 120–129.

Lu, Y., Wang, L., 2021. How to automate timely large-scale mangrove mapping with remote sensing. Remote Sens. Environ. 264, 112584.

Marcos, D., Volpi, M., Kellenberger, B., Tuia, D., 2018. Land cover mapping at very high resolution with rotation equivariant CNNs: Towards small yet accurate models. ISPRS J. Photogramm. Remote Sens. 145, 96–107.

Masemola, C., Cho, M.A., Ramoelo, A., 2020. Sentinel-2 time series based optimal features and time window for mapping invasive Australian native Acacia species in KwaZulu Natal, South Africa. Int. J. Appl. Earth Obs. Geoinf. 93.

Merzlyak, M.N., Gitelson, A.A., Chivkunova, O.B., Rakitin, V.Y., 1999. Non-destructive optical detection of pigment changes during leaf senescence and fruit ripening. Physiol. Plant. 106, 135–141.

Moreau, S., Bosseno, R., Gu, X.F., Baret, F., 2003. Assessing the biomass dynamics of Andean bofedal and totora high-protein wetland grasses from NOAA/AVHRR. Remote Sens. Environ. 85, 516–529.

Mura, M.D., Benediktsson, J.A., Bovolo, F., Bruzzone, L., 2008. An unsupervised technique based on morphological filters for change detection in very high resolution images. IEEE Geosci. Remote Sens. Lett. 5, 433–437.
Ni, R.G., Tian, J.Y., Li, X.J., Yin, D.M., Li, J.W., Gong, H.L., Zhang, J., Zhu, L., Wu, D.L., 2021. An enhanced pixel-based phenological feature for accurate paddy rice mapping with Sentinel-2 imagery in Google Earth Engine. ISPRS J. Photogramm. Remote Sens. 178, 282–296.
Noonan, M., Chafer, C., 2007. A method for mapping the distribution of willow at a catchment scale using bi-seasonal SPOT5 imagery. Weed Res. 47, 173–181.
Pastor-Guzman, J., Dash, J., Atkinson, P.M., 2018. Remote sensing of mangrove forest phenology and its environmental drivers. Remote Sens. Environ. 205, 71–84.
Pu, R., Landry, S., Yu, Q., 2018. Assessing the Potential of Multi-Seasonal High Resolution Pleiades Satellite Imagery for Mapping Urban Tree Species, 5th International Workshop on Earth Observation and Remote Sensing Applications (EORSA). Xian, PEOPLES R CHINA, pp. 1–5.
Pulford, I., Watson, C., 2003. Phytoremediation of heavy metal-contaminated land by trees—a review. Environ. Int. 29, 529–540.
Rana, P., Gautam, B., Tokola, T., 2016. Optimizing the number of training areas for modeling above-ground biomass with ALS and multispectral remote sensing in subtropical Nepal. Int. J. Appl. Earth Obs. Geoinf. 49, 52–62.
Savitzky, A., Golay, M.J., 1964. Smoothing and differentiation of data by simplified least squares procedures. Anal. Chem. 36, 1627–1639.
Schmidt, K.S., Skidmore, A.K., 2003. Spectral discrimination of vegetation types in a coastal wetland. Remote Sens. Environ. 85, 92–108.
Shi, W., Guo, D., Zhang, H., 2022. A reliable and adaptive spatiotemporal data fusion method for blending multi-spatiotemporal-resolution satellite images. Remote Sens, Environ, p. 268.
Sun, W., Wang, R., 2018. Fully Convolutional Networks for Semantic Segmentation of Very High Resolution Remotely Sensed Images Combined With DSM. IEEE Geosci. Remote Sens. Lett. 15, 474–478.
Tian, J.Y., Wang, L., Yin, D.M., Li, X.J., Diao, C.Y., Gong, H.L., Shi, C., Menenti, M., Ge, Y., Nie, S., Ou, Y., Song, X.N., Liu, X.M., 2020. Development of spectral-phenological features for deep learning to understand Spartina alterniflora invasion. Remote Sens. Environ. 242, 15–15.
Tian, J., Wang, L., Li, X., Gong, H., Shi, C., Zhong, R., Liu, X., 2017. Comparison of UAV and WorldView-2 imagery for mapping leaf area index of mangrove forest. Int. J. Appl. Earth Obs. Geoinf. 61, 22–31.
Tolpekin, V.A., Stein, A., 2009. Quantification of the Effects of Land-Cover-Class Spectral Separability on the Accuracy of Markov-Random-Field-Based Superresolution Mapping. IEEE Trans. Geosci. Remote Sens. 47, 3283–3297.
Tonbul, H., Colkesen, I., Kavzoglu, T., 2020. Classification of poplar trees with object-based ensemble learning algorithms using Sentinel-2A imagery. Journal of Geodetic Science 10, 14–22.
Tucker, C.J., 1979. RED AND PHOTOGRAPHIC INFRARED LINEAR COMBINATIONS FOR MONITORING VEGETATION. Remote Sens. Environ. 8, 127–150.
Wan, X., Gu, G., Lei, M., Zeng, W., 2020. Bioaccessibility of metals/metalloids in willow catkins collected in urban parks of Beijing and their health risks to human beings. Science of the Total Environment 717.
Wang, C.K., Chang, L.-W., 2019. Semantic Segmentation via Global Convolutional Network and Concatenated Feature Maps. ICPRAM 292–297.
Wang, T., Zhang, H., Lin, H., Fang, C., 2016. Textural-Spectral Feature-Based Species Classification of Mangroves in Mai Po Nature Reserve from Worldview-3 Imagery. Remote Sensing 8.
Wang, L., Silvan-Cardenas, J.L., Yang, J., Frazier, A.E., 2013. Invasive Saltcedar (Tamarisk spp.) Distribution Mapping Using Multiresolution Remote Sensing Imagery. Professional Geographer 65, 1–15.
Wang, X., Wang, L., Tian, J., Shi, C., 2021. Object-based spectral-phenological features for mapping invasive Spartina alterniflora. Int. J. Appl. Earth Obs. Geoinf. 101.
Wen, D., Huang, X., Bovolo, F., Li, J., Ke, X., Zhang, A., Benediktsson, J.A., 2021. Change Detection From Very-High-Spatial-Resolution Optical Remote Sensing Images: Methods, applications, and future directions. IEEE Geosci. Remote Sens. Mag. 9, 68–101.
Wu, Y., Xiao, X., Chen, R., Ma, J., Wang, X., Zhang, Y., Zhao, B., Li, B., 2020. Tracking the phenology and expansion of Spartina alterniflora coastal wetland by time series MODIS and Landsat images. Multimedia Tools and Applications 79, 5175–5195.
Xiao, X., Boles, S., Frolking, S., Salas, W., Moore, B., Li, C., He, L., Zhao, R., 2002. Observation of flooding and rice transplanting of paddy rice fields at the site to landscape scales in China using VEGETATION sensor data. Int. J. Remote Sens. 23, 3009–3022.
Xiao, X.M., Hollinger, D., Aber, J., Goltz, M., Davidson, E.A., Zhang, Q.Y., Moore, B., 2004. Satellite-based modeling of gross primary production in an evergreen needleleaf forest. Remote Sens. Environ. 89, 519–534.
Yan, H., Xiao, X., Huang, H., 2010. Satellite observed crop calendar and its spatio-temporal characteristics in multiple cropping area of Huang-Huai-Hai Plain. Acta Ecologica Sinica 30, 2416–2423.
Zeng, L., Wardlow, B.D., Xiang, D., Hu, S., Li, D., 2020. A review of vegetation phenological metrics extraction using time-series, multispectral satellite data. Remote Sens, Environ, p. 237.
Zhang, H., Fritts, J.E., Goldman, S.A., 2008. Image segmentation evaluation: A survey of unsupervised methods. Comput. Vis. Image Underst. 110, 260–280.
Zhang, H., Wang, T., Liu, M., Jia, M., Lin, H., Chu, L.M., Devlin, A.T., 2018. Potential of Combining Optical and Dual Polarimetric SAR Data for Improving Mangrove Species Discrimination Using Rotation Forest. Remote Sensing 10.
Zhang, M., Zhang, H., Li, X., Liu, Y., Cai, Y., Lin, H., 2020. Classification of Paddy Rice Using a Stacked Generalization Approach and the Spectral Mixture Method Based on MODIS Time Series. IEEE J. Sel. Top. Appl. Earth Obs. Remote Sens. 13, 2264–2275.
Zhou, D., Zhao, S., Zhang, L., Liu, S., 2016. Remotely sensed assessment of urbanization effects on vegetation phenology in China's 32 major cities. Remote Sens. Environ. 176, 272–281.